Effect of 3D Roughness Patch on Instability Amplification in a Supersonic Boundary Layer

Meelan Choudhari[*] and Fei Li[†]
NASA Langley Research Center, Hampton, VA, 23681

Pedro Paredes[‡]
National Institute of Aerospace, Hampton, VA, 23663

Lian Duan[§]
Missouri University of Science and Technology, Rolla, MO, 65409

   Surface roughness is known to have a substantial impact on the aerothermodynamic loading of high-speed vehicles, particularly via its influence on the laminar-turbulent transition process within the boundary layer. Numerical simulations are performed to investigate the effects of a distributed region of densely packed, sinusoidal shape roughness elements on a Mach 3.5 flat plate boundary layer for flow conditions corresponding to the planned conditions of an upcoming experiment in the Mach 3.5 Supersonic Low Disturbance Tunnel at the NASA Langley Research Center. Analysis of convective instabilities in the wake of the roughness patch was reported in a previous paper and the current work extends that analysis to instability amplification across the length of the roughness patch. Quasiparallel stability analysis of the modified boundary layer flow over the patch indicates two dominant families of unstable disturbances, namely, a group of high frequency modes that amplify in localized regions along the roughness patch and another group of low frequency modes that have smaller peak amplification rates but amplify steadily both above the roughness patch and in the wake region behind it. The results suggest that the amplification factors associated with the high-frequency modes are sufficiently low, at least for the roughness patches considered in this paper, so that these modes are unlikely to have a major influence on the transition process. The amplification of the low-frequency modes within the region of the roughness patch is further quantified via direct numerical simulations. Results confirm the strongly destabilizing influence of the roughness patch on the first mode instabilities, yielding an N-factor increment of $\Delta N \approx 3.6$ for a roughness patch length of eight wavelengths.

Nomenclature

A_u = nondimenisonal streak amplitude based on streamwise velocity
D = diameter of cylindrical roughness element [m]
f = frequency of instability waves [kHz]
h = distribution of surface height perturbation associated with roughness patch
k = peak height of roughness elements [m]
L_w = streamwise length of wall roughness patch
M_∞ = freestream Mach number
N = logarithmic amplification ratio relative to a reference location
P_∞ = freestream pressure [Pa]
Re = freestream unit Reynolds number [m^{-1}]
t = time [sec]
T_{ad} = adiabatic wall temperature [K]
T_w = wall temperature [K]

---

[*] Aerospace Technologist, Meelan.M.Choudhari@nasa.gov, Associate Fellow, AIAA.
[†] Aerospace Technologist, Fei.Li@nasa.gov
[‡] Research Engineer, pedro.paredes@nasa.gov, Senior Member, AIAA.
[§] Assistant Professor, lduan@mst.edu, Senior Member, AIAA.

T_∞	=	freestream temperature [K]
u	=	streamwise velocity [m/s]
u_s	=	spanwise varying component of perturbation in stationary streamwise velocity [m/s]
u'	=	streamwise velocity fluctuation [m/s]
U_∞	=	freestream velocity [m/s]
x	=	axial coordinate [m] or [mm]
x_0	=	axial coordinate corresponding to beginning of roughness patch [m] or [mm]
y	=	wall-normal distance [m] or [mm]
z	=	spanwise coordinate [m] or [mm]
ζ	=	interger valued computational coordinate along the spanwise diretion
δ	=	boundary layer thickness [m]
λ_w	=	streamwise wavelength of roughness patch [m] or [mm]
λ_z	=	spanwise wavelength of roughness patch [m] or [mm]
σ	=	spatial amplification rate [m^{-1}]

I. Introduction

Boundary layer transition from the laminar to a turbulent state is known to have a major impact on the design and performance of high-speed flight vehicles. When the vehicle surface is relatively smooth, the transition process is initiated by linear instabilities of the laminar boundary layer, including streamwise instabilities in the form of first and second (or Mack) mode instabilities, Görtler instabilities associated with centrifugal effects due to concave curvature of the boundary layer streamlines, and stationary and/or traveling modes of crossflow instability in three-dimensional boundary layers. Transition may also occur right along the leading edge of an aerodynamic surface, either as a result of streamwise instabilities of the attachment line boundary layer or due to a form of "bypass" transition caused by the convection of high-amplitude fluctuations from juncture regions involving turbulent flow over an adjacent surface such as a vehicle fuselage.

In practice, the above-mentioned transition scenarios can be significantly altered by the frequent occurrence of surface roughness over real flight vehicles. Here, the term surface roughness is used in a broad sense to denote all short-scale variations in surface geometry that would invalidate the assumptions of the classical boundary layer theory by introducing rapid spatial gradients in the flowfield adjacent to the surface. The geometry variations may be either local (i.e., discrete, isolated roughness elements) or nonlocal (i.e., distributed) in their spatial extent. Furthermore, the surface height distribution may vary along a single direction along the surface (i.e., 2D roughness) or can be a function of both surface coordinates (i.e., 3D roughness). The magnitude of height perturbations may range from rather small values such that the roughness crests are buried deep within the boundary layer, to rather large magnitudes where the roughness contour extends well beyond the edge of the unperturbed boundary layer. Other significant roughness attributes include its length scales along both crossflow and streamwise directions (with the ratio of these two length scales denoting the planform aspect ratio of representative elements), shape, and orientation with respect to the inviscid streamline. Depending on the uncertainties related to the underlying cause for the surface roughness and/or the geometric complexity of the roughness height distribution, the latter may not always be fully deterministic and, at times, may need to be treated as either partially or fully stochastic in nature.

Examples of discrete roughness elements encountered in practical applications include protuberances or cavities that arise as a byproduct of the structural design of the vehicle or as a result of damage to the heat shield due to debris impact during vehicle launch, and gap fillers protruding in between the tiles of the thermal protection system (TPS). Other examples of surface roughness include: distributed surface imperfections due to spallation or nonuniform surface recession over an ablative heat shield or due to misalignment of steps and gaps between the tiles of a TPS surface; other manufacturing imperfections such as surface waviness, and steps or gaps created during the assembly of different components; or due to differential thermal expansion during the flight, and arrays of discrete roughness elements that are deployed as tripping devices over the forebody of hypersonic vehicles with scramjet propulsion.

In general, the presence of surface roughness can influence the aerothermodynamics of high-speed vehicles in two different ways. If the approaching boundary layer flow is already turbulent, then the presence of surface roughness can augment the heat flux associated with the turbulent flow. On the other hand, when the incoming boundary-layer flow is laminar, the presence of 3D surface roughness tends to accelerate the laminar-turbulent transition process. Because boundary layer transition can increase the surface heating rates by a factor of nearly four to eight, roughness effects become very important when they cause the transition front to move close to the leading

edge (or the nose) of the vehicle surface. Premature transition on reentry vehicles can jeopardize the structural integrity of the entire vehicle and pose a major safety hazard as shown by the investigations related to the 2005 accident involving the shuttle orbiter Columbia.[1] While roughness-induced tripping of the boundary layer leads to undesirable consequences in a number of practical applications, artificial roughness elements are often employed in scramjet applications to intentionally trip the boundary layer on the forebody of the vehicle to prevent engine unstart without producing unacceptable levels of flow nonuniformities at the entrance to the combustor inlet.

Empirical observations involving discrete roughness elements[2,3] have identified the maximum roughness height as the dominant parameter controlling the effects on the laminar-turbulent transition process. Measurements suggest that when the roughness height exceeds a critical value, the transition front begins to move upstream relative to that over a smooth surface in the same disturbance environment. The rate of upstream movement slows down at sufficiently large heights and, for roughness heights larger than the so-called effective trip height, the onset of transition appears to asymptote to a location that may range from just behind the roughness element to a finite distance downstream. Both the critical and effective values of the roughness height parameter are influenced by the shape of the roughness element, and also by the external disturbance environment as demonstrated by the recent experiments in the Mach 6 quiet tunnel at Purdue University.[3]

Despite the common occurrence of surface roughness and its well-known impact on the vehicle design and operation for high-speed flight, the physical mechanisms underlying the transition process behind discrete roughness elements were not understood for a long time. Consequently, predictions in practical applications were based on empirical prediction criteria derived from measurement databases involving limited data from prior flights and supplementary measurements in conventional wind tunnel facilities. The extensive research performed in support of the shuttle orbiter Discovery's Return-To-Flight (RTF) led to a first generation, rapid predictive capability for boundary layer transition due to damage or repair to the thermal protection system.[1] The usefulness of such empirical methodology is, however, limited by the significant uncertainty associated with the correlation and the fact that it cannot be reliably extrapolated beyond the limited underlying database. Often, the vehicle design process is based on the assumption of fully turbulent flow (e.g., the X-34 and Orion Multipurpose Crew Vehicles). Such an overly conservative design approach leads to thicker than necessary TPS and increased total weight or, equivalently, reduced payload fraction.

For overviews of earlier research related to roughness effects on transition including both slender/aerodynamic and blunt body configurations, the reader is referred to the reviews by Schneider.[4,5] More recent research under the NASA Fundamental Aeronautics Program led to significant breakthroughs in the understanding of physical mechanisms responsible for transition due to discrete roughness elements and has also provided constituents toward a next generation, physics-based prediction tool. With sustained effort, a prediction capability of this type could be incorporated into the aerothermodynamic assessment of a broader class of hypersonic vehicles. An overview of the lessons learned from these research efforts was presented by Choudhari et al.[6]

Naturally occurring surface nonuniformities, such as the roughness shapes induced by surface ablation, tend to be spatially distributed in nature. Thus, one must investigate the effects of spatial proximity between different parts of the roughness distribution. In that regard, the simplest configuration consists of multiple, discrete roughness elements, with the downstream elements located within the wakes of the upstream elements.[7,8] The most complex case involves densely packed roughness distribution with a potentially heterogeneous mixture of roughness scales, sizes, and orientations.[9–12] A configuration of intermediate complexity involves smooth-shaped, sinusoidal roughness elements distributed over multiple wavelengths.[13] Specifically, Muppidi et al.[13] studied a relatively simple distributed roughness configuration involving a linear superposition of two waves that are inclined at equal but opposite angles with respect to the freestream direction underneath a Mach 2.9 flat plate boundary layer. Since the roughness patch wavelengths along the streamwise and spanwise directions were nearly the same, the resulting surface shape resembled a potentially shallower version of the surface of an egg carton. No unsteady disturbances were introduced in their simulation, but the flow developed spontaneous instabilities that led to transition just behind the roughness patch.

In a recent paper,[14] we reported on numerical computations of similar, distributed roughness configurations in the context of a Mach 5.3 boundary layer over a 7-deg. half-angle circular cone and a Mach 3.5 flat plate boundary layer. Whereas the flow conditions and surface temperature distribution for the Mach 5.3 configuration were selected to model the $t = 21.5$ second trajectory point during the HIFiRE-1 flight experiment,[15] the flow conditions for the Mach 3.5 flat-plate configuration were chosen on the basis of the related experiments by Chou et al.[8] in the Supersonic Low Disturbance Tunnel at the NASA Langley Research Center. In the absence of surface roughness, the Mach 5.3 boundary layer supports strong amplification of second mode (i.e., Mack mode) instability waves so that transition onset occurs near 83 percent of the body length. On the other hand, the Mach 3.5 boundary layer supports relatively weak amplification of first mode instabilities, and hence, transition over a smooth plate was not

expected to occur within the length of the model. Thus, together, these two configurations provided a reasonably broad context for investigating the effects of a smooth-shaped distributed roughness configuration.

   The emphasis of the earlier work[14] was on the boundary layer distortion within the wake of the roughness patch and the development of modal instabilities within the wake region. Thus, the development of instability waves over the length of the roughness patch was not considered. The present study, which may be regarded as a sequel to Ref. [14], is designed to investigate that initial phase of the overall disturbance evolution. This initial development above the roughness patch may be expected to become more significant as the patch length increases, i.e., when the ratio of the roughness patch length to its distance from the leading edge becomes $O(1)$, and especially for sufficiently large roughness height perturbations. Section II describes the boundary layer modification due to selected roughness configurations. Predictions of instability characteristics within the length of the roughness patch based on a locally parallel assumption are presented first in Section III. Because of the strongly nonparallel nature of the flowfield above the patch, such quasiparallel predictions are expected to provide, at best, some limited insights into the nature of the flow instability. This analysis was also used to guide the choice of disturbance parameters for the direct numerical simulations (DNS) of disturbance evolution above the patch, which are described in the latter part of Section III. Disturbance growth within the roughness patch region is compared with the previously reported amplification factors within the wake region.[14] Brief concluding remarks are presented in Section IV.

II.   Roughness Configurations and Base Flow Modification

A. Roughness Configurations
   Following Ref. [14], we continue the study of a relatively simple distributed roughness configuration over a flat plate that involves deterministic and smooth surface height variations over a spatially extended region. This configuration is modeled after the roughness geometry considered in the computations of Muppidi et al.,[13] who examined the effects of sinusoidal height variations comprised of a linear superposition of two waves that are inclined at equal but opposite angles with respect to the freestream direction. The surface height perturbation used in their study corresponds to

$$h(x, z) = k \sin(2\pi x/\lambda_w) \cos(2\pi z/\lambda_z), \tag{1}$$

which may also be viewed as multiple spanwise arrays of smoothly shaped roughness elements that are staggered in the streamwise direction. At the primary flow conditions of $M_\infty = 2.9$, $Re = 25\times10^6$/m, $k/\delta = 0.30$ and $\lambda_w/\delta = 3.375$ ($\lambda_w = 2.54$ mm) at the beginning of the surface waviness, and $T_w/T_{ad} = 1$, the computed flow became unsteady without any external forcing. The fundamental wavelength of the surface height distribution had very similar values in the streamwise and spanwise directions, respectively. Computations revealed that both skin friction and surface heat transfer began to rise rather rapidly just past the end of roughness, and reached their respective peak values at a distance of approximately $10\lambda_w$ downstream of the aft end of the roughness strip. Flow above the roughness region was characterized by the presence of both a shear layer with strong velocity gradients at a finite height above the wavy surface and a spanwise periodic array of streamwise vortices that developed below the shear layer. Analysis of the computed data also showed that the spatial variations in the wall-normal velocity gave rise to streamwise vorticity that gained in strength with distance along the roughness strip, and also induced streamwise streaks of alternating high and low velocity. Muppidi et al.[13] argued that the streamwise vortices were a critical part of the transition mechanism in this case and that it was the interaction between these vortices and the shear layer that initiated the laminar breakdown in the flow.

   Again, building upon the work described in our previous paper,[14] we investigate the effects of a roughness patch given by Eq. 1 on a Mach 3.5 flat plate boundary layer for flow conditions that are relevant to a future experiment in the Supersonic Low Disturbance Tunnel (SLDT) at the NASA Langley Research Center. The nominal freestream conditions selected for the present computations are identical to those in Ref. [14], which are also close to the flow condition from the previous measurements involving discrete roughness elements in the work of Chou et al.,[8] namely, $P_\infty = 2719.9$ Pa, $T_\infty = 92.55$ K, with a unit Reynolds number of 10.77×10^6 per meter. The model surface temperature is assumed to be uniform along the length of the plate and equal to $T_w = 290$ K.

   Chou et al.[8] had reported roughness wake measurements at similar flow conditions for roughness configurations with multiple, isolated elements. They found that a cylindrical roughness element with a diameter of $D = 3.58$ mm and height $k = 140$ μm (i.e., $k/\delta \approx 0.2$) at a distance of 41.5 mm downstream from the leading edge led to the amplification of an antisymmetric instability mode within the wake region; however, that amplification was insufficient to produce transition within the measurement region. When the roughness element height was increased to $k = 280$ μm (i.e., $k/\delta \approx 0.4$), a symmetric instability mode amplified more rapidly in the wake region, resulting in the onset of transition within the length of the plate. For multiple roughness elements aligned in the streamwise

direction, an interelement spacing of 4*D* yielded substantially stronger mean wake distortion in comparison with a single roughness element. However, a roughness element spacing of 2*D* was found to be too small to yield an effective constructive interference between the wake disturbances induced by the roughness elements in tandem.

Table 1 outlines the geometry of the various roughness patch configurations considered in this study and a limited body of results pertaining to a selected subset of these configurations was presented in the previous paper [14]. Similar to Ref. [14], the primary focus of the analysis corresponds to the case with $\lambda_w = \lambda_z = 6.25$ mm, which corresponds to a half wavelength (i.e., protuberance portion within a single wavelength) of 3.25 mm. See Fig. 1 for the schematic of a roughness patch with $L_w/\lambda_w = 4.0$. While the half wavelength of a sinusoidal distribution is not exactly equivalent to the diameter of a discrete, cylindrical roughness element, it may be seen that the half wavelength in the present case is comparable to the roughness diameter of 3.58 mm from the previous SLDT experiment for cylindrical roughness elements.[8] Based on the roughness patch location envisioned for the follow-on measurements in the future, the roughness patch in all of the computations begins near $x = 0.0288$ m (where the local boundary layer thickness is slightly less than 0.6 mm), with the patch length ranging from $L_w/\lambda_w = 0.5$ to $L_w/\lambda_w = 8.0$ and the roughness height is held fixed at $k = 272$ μm. Limited computational results involving a range of roughness heights from $k = 68$ μm up to $k = 340$ μm have been presented earlier in Ref. [14]. The roughness height selected in the present paper is close to the $k = 280$ μm height of the discrete (cylindrical) roughness elements considered in the measurements by Chou et al.[8] For the longer roughness patches of interest in this paper (i.e., $L_w/\lambda_w \geq 4$), the length of the roughness patch is nearly the same or even greater than the distance between the plate leading edge and the beginning of the patch. As explained in Ref. [14], the thickness of the unperturbed boundary layer varies more than 35 percent over the length of the patch, and for that reason, we have chosen to characterize the patch height in absolute units, rather than as the nondimensional parameter k/δ.
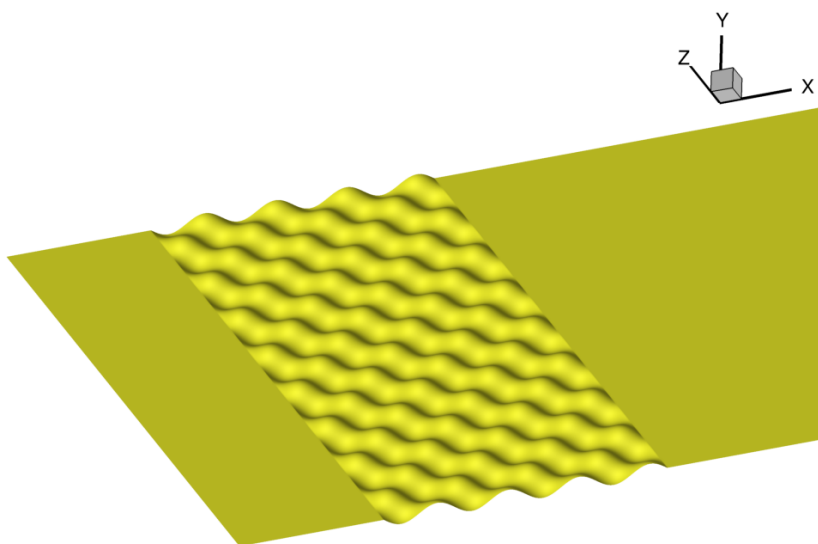
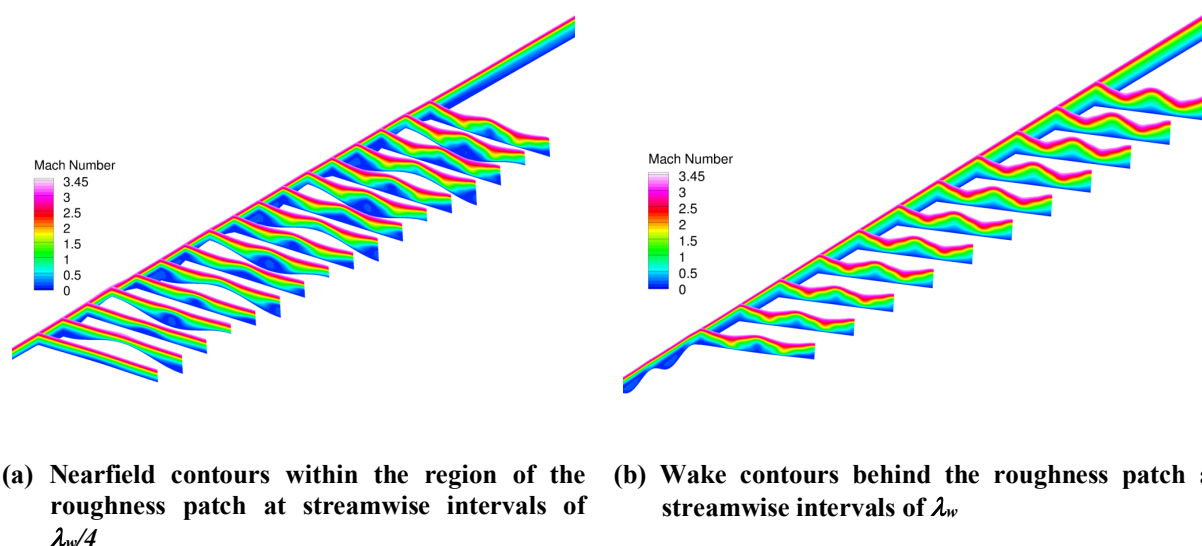**Figure 1. Schematic of a roughness patch with $L_w/\lambda_w = 4.0$ from Table I.**

Table 1 Roughness patches investigated for Mach 3.5 flat plate.

k, μm	λ_w, mm	λ_z, mm	L_w/λ_w
272	6.25	6.25	0.5, 1.0, 2.0, 4.0, 8.0
340	6.25	6.25	0.5, 1.0, 2.0, 4.0, 8.0, 12.0
136, 272	1.7	6.25	15.0
68, 136, 204, 272	6.25	1.7	4.0
272	4.2	4.2	6.0
272	3.125	3.125	8.0
68, 102, 136, 204, 272	1.7	1.7	15.0

American Institute of Aeronautics and Astronautics

B. Mach 3.5 Flat Plate Boundary Layer in the Presence of a Roughness Patch

In the interest of enabling an efficient parametric study that will provide guidance for a future experiment involving a patch of surface waviness, a production CFD code in the form of the VULCAN (Viscous Upwind aLgorithm for Complex flow ANalysis)[16] software was used by Choudhari et al.[14] to compute the basic state flow distortion due to the patches of distributed surface roughness. The VULCAN code solves the unsteady, conservation equations appropriate for laminar or turbulent flow of calorically or thermally perfect gases with a spatially second-order accurate cell-centered finite-volume scheme. For the roughness patch computations, the inviscid fluxes were constructed using the MUSCL $\kappa = 0$ scheme, the van Albada gradient limiter[17] and the Low Dissipation Flux Split Scheme (LDFSS) of Edwards.[18,19] The cell face gradients required to construct the viscous fluxes were obtained using an auxiliary control volume approach that results in a compact viscous stencil that produces a second-order accurate approximation of the full Navier-Stokes viscous fluxes. A typical grid used in the computations described herein involved 6720×120×720 points in the streamwise, spanwise, and wall-normal directions, respectively. Additional computations were performed with grids that were coarser by a factor of 1.5 in each direction to ensure that the computed flow solutions showed minor changes in the predicted wake distortions.

Mach number contours in y-z planes at selected stations for the case of $\lambda_w = \lambda_z = 6.25$ mm, $L_w/\lambda_w = 4.0$, $k = 272$ μm were presented in Ref. 14 and are reproduced in Fig. 2 below. Figure 2(a) reveals the flow evolution within the region of the roughness patch, whereas Mach number contours in the wake region behind the roughness patch are shown in Fig. 2(b). As described in Ref. [14], Mach number contours near the centerplane ($z = 0$) in Fig. 2(a) indicate the cyclic pattern of flow acceleration over the rising segments of the surface topography and retardation over the lee side of those segments. Concomitantly, one observes a progressive build up in the size of the blue shaded region within the troughs of successive wavelengths of the roughness patch, which gives rise to increased boundary layer thickness along the symmetry planes at $z/\lambda_z = \pm 0.5j$, with j being an arbitrary integer. The spanwise undulations in streamwise velocity distribution are sustained in the wake region behind the roughness patch, giving rise to similar streaks as those observed behind a single array of roughness elements.[20] Even though pockets of reversed flow exist within the valley regions, i.e., recesses within the roughness patch, the magnitude of reversed flow velocity is rather small, typically less than five percent of the freestream velocity.

(a) Nearfield contours within the region of the roughness patch at streamwise intervals of $\lambda_w/4$

(b) Wake contours behind the roughness patch at streamwise intervals of λ_w

Figure 2. Mach number contours at selected stations above and behind the roughness patch with $\lambda_w = 6.25$ mm, $k = 272$ μm, and $L_w/\lambda_w = 4.0$.[14] The contours at each streamwise station cover a spanwise interval of $z/\lambda_z = $ [-0.5, 0.5]. For reference, the streamwise evolution of flow within the $z/\lambda_z = -0.5$ plane is also shown along the left boundary of the plot.

Although not shown, the flowfield over the first half of the roughness patch with $L_w/\lambda_w = 8.0$ is very similar to that presented in Ref. [14]. As discussed in that earlier work, the separation surface (i.e., boundary of the reversed flow region) consists of a sequence of narrow, finite-length sawtooth like structures, or ridges, that are aligned in the

streamwise direction and, hence, cause the higher velocity fluid to go around these ridges, giving rise to the observed streaks in the flow over the rough region. The spanwise variations continue to gain in strength along the length of the roughness patch. As a result, the velocity amplitude of the streak at the beginning of the wake region is considerably stronger for the longer roughness patch with $L_w/\lambda_w = 8.0$. The progressive intensification of streaks over the roughness region, coupled with a decay in streak amplitudes behind the roughness strip as discussed later, suggests that the boundary layer is likely to support a strong disturbance growth even within the region of waviness, as opposed to mostly in the wake region in the case of discrete, isolated roughness elements.[6,7]

Axial evolution of the streak amplitude associated with the modified boundary layer flow is plotted in Fig. 3(a) for three different lengths of the roughness patch, while the peak roughness height is held fixed at $k = 272$ μm. The streak amplitude is defined as

$$A_u(x) = 0.5 * [max(u_s(x,y,z)) - min(u_s(x,y,z))] \qquad (2)$$

where u_s denotes the spanwise varying component of the stationary perturbation in the basic state streamwise velocity (i.e., local u velocity minus its spanwise average) and both the maximum and the minimum are evaluated across the y-z plane at each streamwise station. The rapid oscillations in $A_u(x)$ within the initial section of each curve correspond to the roughness patch region. Because of the spanwise variation in the surface height distribution within this portion of the plate surface, the spanwise average is computed as a discrete mean over the computational coordinate ζ, which is nominally aligned with the spanwise direction. As a result, the computed streak amplitude within the roughness region does not have any physical significance; however, it is included in the figure simply to highlight the streamwise extent of the roughness patch. Observe that the peak value of the streak amplitude occurs at the end of the roughness patch, i.e., at the beginning of the wake region. The results from Fig. 3(a) highlight the increase in the maximum value of the streak amplitude as the roughness patch length is increased from $L_w/\lambda_w = 1.0$ to $L_w/\lambda_w = 8.0$. However, the rate of increase in the peak amplitude at the beginning of the wake appears to diminish with each increase in L_w/λ_w. Furthermore, for the roughness patches considered in Fig. 3(a), the relative increase in the streak amplitude is much smaller than the underlying increment in L_w/λ_w. On the other hand, an increasing roughness patch length implies a proportionately longer region of highly disturbed flow above the patch, which is likely to result in a substantial increase in the instability amplification across the roughness region.

Figure 3(b) illustrates the comparison of streak amplitude evolution for two different spanwise wavelengths of the surface waviness. This comparison indicates that the smaller spanwise wavelength ($\lambda_z = 1.7$ mm) leads to a strong reduction in the peak value of A_u as well as to a more rapid decay in the streak amplitude along the wake.

(a) Effect of roughness patch length L_w/λ_w (b) Effect of spanwise wavelength λ_z
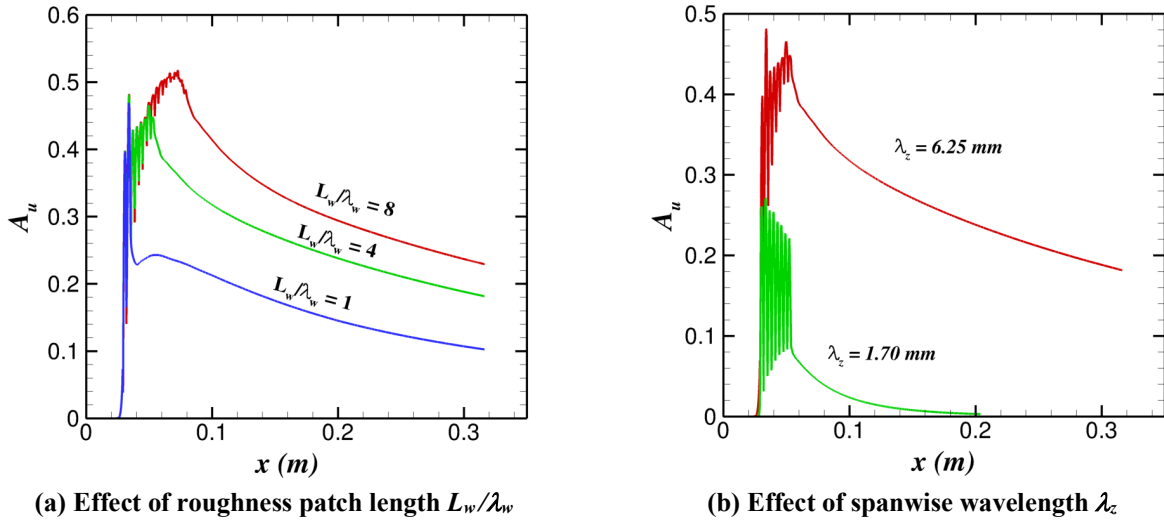
Figure 3. Streak amplitude evolution for different roughness configurations with varying patch length L_w/λ_w and spanwise wavelength λ_z. (The roughness height $k = 272$ μm and streamwise wavelength $\lambda_w = 6.25$ mm are held fixed in all cases.)

American Institute of Aeronautics and Astronautics

III. Disturbance Evolution over Roughness Patch

As seen from the results in Figs. 2 and 3, the flow distortion due to the roughness patch can persist for long distances within the wake region. However, the disturbance amplitude decays approximately monotonically throughout the length of the wake. Because of the relatively slow streamwise variations in the wake structure, the flow instabilities within the wake region can be analyzed on a local (i.e., quasicylindrical) basis by using a planar stability analysis at each streamwise location, similar to that behind a single array of discrete roughness elements [20–22]. On the other hand, the streamwise variation in the boundary layer flow includes a cyclic component within the roughness patch region, which varies on the scale of the streamwise wavelgnth λ_w. As a result of these shorter-scale variations, stability analysis of the boundary layer flow over the roughness patch becomes considerably more complex than the quasiparallel instability analysis of the wake flow in Ref. [14]. A comprehensive analysis of the flow instabilities over the roughness patch region is still ongoing and a preliminary set of results is presented in the current paper.

To begin with, we will use a local stability analysis to gain limited insights into the nature of flow instability within the roughness patch, keeping in mind the theoretical shortcoming of this approach as mentioned in the preceding paragraph. Following this analysis, direct numerical simulations of unsteady disturbances are used to obtain more definitive estimates of disturbance amplification above the roughness patch. A Floquet type instability analysis of the fully 3D basic state (which leads to an eigenvalue problem based on 3D partial differential equations) was also performed for unit sections encompassing a single streamwise wavelength of the roughness patch. However, this approach requires a manipulation of the quasiperiodic basic state in order to render it perfectly periodic across each streamwise wavelength, which led to rather significant changes in the original basic state. As a result, findings from the Floquet analysis are not included in the present paper.

A. Modal Amplification along the Roughness Patch

The contour plots in Fig. 2(a) for the roughness patch with $\lambda_w = 6.25$ mm, $k = 272$ μm, and $L_w/\lambda_w = 4.0$ indicate that the effects of streamwise undulations in the surface contour are mainly manifested in the low-speed region close to the solid surface, as indicated by the blue shaded portions of the velocity contours. This inner, low-speed region expands and contracts in a cyclic manner, with a streamwise wavelength equal to λ_w. On the other hand, the region of high spanwise shear near the upper edge of the boundary layer structures displayed in these plots reveals a progressive strengthening of the spanwise undulations in boundary layer thickness along the entire length of the roughness patch. These sustained spanwise undulations lead to the development of streamwise streaks with a spanwise scale of $\lambda_z/2$, yielding a pair of streaks across each spanwise wavelength of the roughness patch. Thus, even though the same short-scale variations in the underlying surface contour give rise to both the low- and high-shear regions, the latter region exhibits apparently weaker variations in the streamwise direction in comparison with the streamwise oscillations within the inner, valley regions. Since the instability modes associated with the streaks are typically concentrated in the high-shear region, the finding that this region does not entail strong streamwise variations motivates the use of a quasiparallel analysis to examine the stability of the flow over the roughness patch. Such an analysis is also analogous in spirit to the previous analysis of wake instability behind the roughness patch.[14]

We begin by noting that the unperturbed (i.e., smooth surface) boundary layer flow in the region of the roughness patch is weakly unstable to oblique, first mode instability waves. Amplification characteristics of the first mode instabilities are shown in Fig. 4, which displays the streamwise evolution of the logarithmic amplification ratio, the N-factor, for fixed frequency disturbances for selected spanwise wavelengths ranging from ½ to 2 times the spanwise wavelength of the roughness patch. The flat plate model used in the quiet tunnel experiments at NASA Langley [8] is 0.4064 m long. The results in Fig. 4 indicate that the peak N-factor for first mode waves over the length of this plate is well below the typical range of N-factors that correlates with first-mode transition in a low disturbance environment (i.e., N ≈ 9–10).
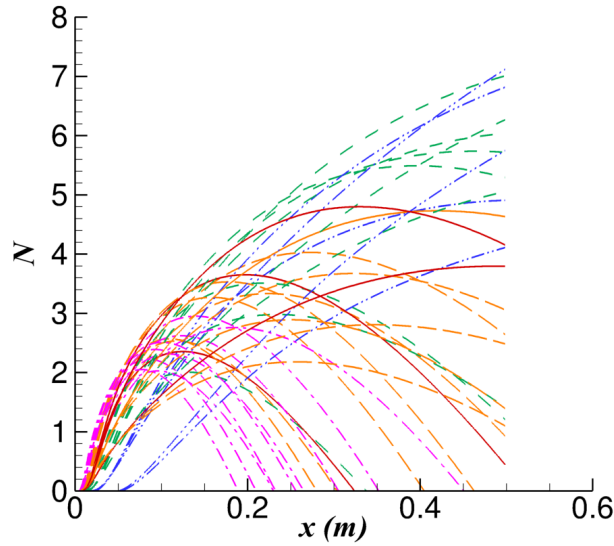
Fig. 4. N-factor evolution based on parabolized stability equations for fixed frequency disturbances at selected spanwise wavelengths ranging from 0.5 to 2 times the spanwise wavelength of the roughness patch. The color of each curve denotes a specific range of frequencies (blue: 10 khz and 20 kHz, green: 30 kHz and 40 kHz, red: 50 kHz, orange: 60 kHz and 70 kHz, purple: 80 kHz and above).

As discussed by Choudhari et al.,[14] the symmetry of the roughness configuration in Eq. (1) across both z/λ_z = -0.5 and z = 0 planes implies that the eigensolutions of linear disturbance equations in the presence of the roughness patch can be classified into 4 different types on the basis of their symmetry characteristics with respect to these two planes. We use the notation of SS, SA, AS, and AA disturbance types depending on whether the instability fluctuations in the wall-normal velocity are symmetric (S) or antisymmetric (A) at z/λ_z = -0.5 and/or z = 0, respectively. Thus, for example, the SA disturbances are symmetric about the z/λ_z = -0.5 plane and antisymmetric with respect to the z = 0 plane. The spanwise wavelength of the SS and AA modes is equal to the fundamental wavelength λ_z of the roughness height distribution from Fig. 1. In contrast, the other two mode types with mixed symmetry conditions may correspond to either a subharmonic mode with a spanwise wavelength equal to twice the fundamental spanwise wavelength of the roughness patch or even a shorter wavelength mode with a spanwise wavelength of two thirds of the fundamental wavelength. Based on the findings of Paredes et al.,[23,24] instability waves that correspond to higher than the first subharmonic of the roughness wavelength have not been considered in the present analysis.

Similar to the wake region behind the roughness patch considered in this section,[14] the flow above the patch can support multiple families of unstable modes within a given category of spanwise symmetry conditions (viz., within each of the categories SS, AA, SA, and AS, respectively). Figures 5(a) through 5(d) display the predicted variation of the local streamwise amplification rates corresponding to the dominant family of disturbances (i.e., those with the highest growth rates) within each mode type. The growth rate for each dominant family is plotted as a function of the disturbance frequency parameter at four different stations that correspond to a streamwise spacing of $\Delta x = \lambda_w/4$ within the last streamwise wavelength from the roughness patch with L_w/λ_w = 4.0 (i.e., the last four planes from Fig. 2(a) ranging from $x \approx$ 49 mm to $x \approx$ 54 mm). Thus, the above four stations represent a successive phase increment of $\pi/2$ radians along the sinusoidal streamwise variation in roughness height as specified in Eq. 1. The growth rate spectra in Fig. 5 reveal two groups of modes, one of which is centered at low frequencies between approximately 30 kHz and 100 kHz and the other group has peak amplification rates at higher frequencies between 200 kHz to 300 kHz. As will be discussed later, the peak velocity fluctuations associated with either group of modes are concentrated in a narrow spanwise region, causing the influence of the neighboring streaks to be relatively small. As a result, each of Figs. 5(a) through 5(d) indicates a pairwise coalescence or near coalescence between the growth rate curves for two different mode types that differ in the spanwise boundary condition at one end. For example, the pair of modes of types SS and SA have nearly the same growth rate variation in Fig. 5(a) across a broad range of frequencies. The peak growth rates of the high-frequency lobes are significantly higher than

9

American Institute of Aeronautics and Astronautics

those of the low-frequency modes. However, the frequency band of the high-frequency modes is relatively narrow, and furthermore, tends to shift from one location to the next as seen from Fig. 5(a). Consequently, the integrated amplification factor of these modes remains fairly small. This conclusion regarding the weak overall amplification of the high frequency modes was supported by the instability analysis of the fully 3D basic state that accounted for both streamwise and spanwise variations across each unit of size $\lambda_x \times \lambda_z$ within the roughnes patch. We also note that the high-frequency instability modes exist only within the region of the roughness patch and were not observed within the wake region.[14]


(a) $j = 0$

(b) $j = 1$

(c) $j = 2$

(d) $j = 3$
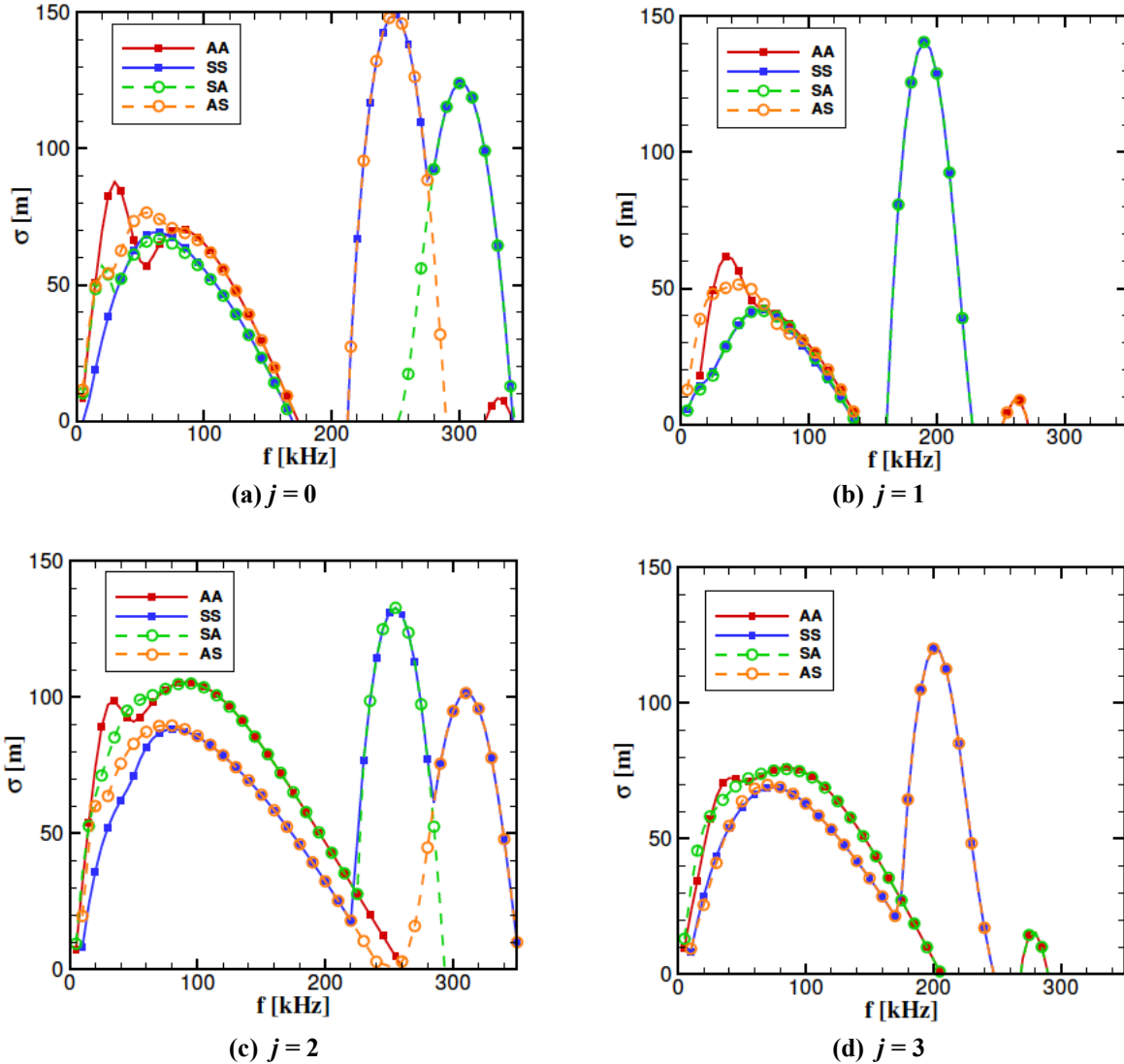
Figure 5. Growth rate variation with respect to frequency at selected streamwise stations corresponding to $x = x_0 + L_w - \lambda_w(1 - j/4)$, $j = 0$–3. Results are shown for the dominant family of unstable disturbances corresponding to spanwise boundary conditions of types SS, AA, SA, and AS, respectively.

On the other hand, the low-frequency group of disturbances amplify steadily (albeit with growth rate component that varies in a cyclical manner) across a majority of the roughness patch and continue their amplification within the wake region downstream. Thus, the evolution of the low-frequency modes over the roughness patch (and, secondarily, also in the region upstream of the patch) increases their overall N-factors beyond the amplification factors predicted by using the instability analysis of the wake region alone. As described in Ref.

[14], the most amplified wake disturbances have frequencies between approximately 40 kHz and 60 kHz, which also fall within the range of the most unstable modes over the roughness patch as seen from Fig. 5. However, because the length of the roughness patch is smaller in comparison with the extended region of amplification within the roughness patch wake and because the peak amplification rates in both regions are comparable to each other, the contribution of the roughness patch to the overall N-factor is expected to be rather modest. Of course, the significance of disturbance growth across the roughness patch is expected to increase when either the roughness patch length and/or the height parameter increases further beyond the corresponding values for the roughness patch under consideration. The variations in peak growth rates of the low-frequency modes across Figs. 5(a) through 5(d) also highlight the need to consider the effects of the streamwise variations in the basic state. We also observe that the frequency range of the low-frequency group of disturbances from Fig. 5 overlaps with the frequency range of oblique, first mode instabilities of the unperturbed boundary layer in Fig. 4. However, the peak growth rates in the presence of the roughness patch are larger than the first mode growth rates at the corresponding locations. This suggests that roughness patch tends to destabilize the first mode disturbances.

The mode shapes of $|u'|$ fluctuations for an AA mode with a fixed frequency of $f = 50$ kHz at the four stations from Fig. 5 are shown in Figs. 6(a) through 6(d), respectively. It may be seen that the peak velocity fluctuations at the $j = 0$ and $j = 1$ locations occur on either side of the symmetry plane at $z/\lambda_z = \pm 0.5$, whereas the modal peak gradually shifts toward the outer symmetry planes at $z = 0$ for the $j = 2$ and $j = 3$ locations. The mode shape variation within each streamwise wavelength from the roughness patch is accompanied by a variation in the amplification rate as seen from Fig. 5.
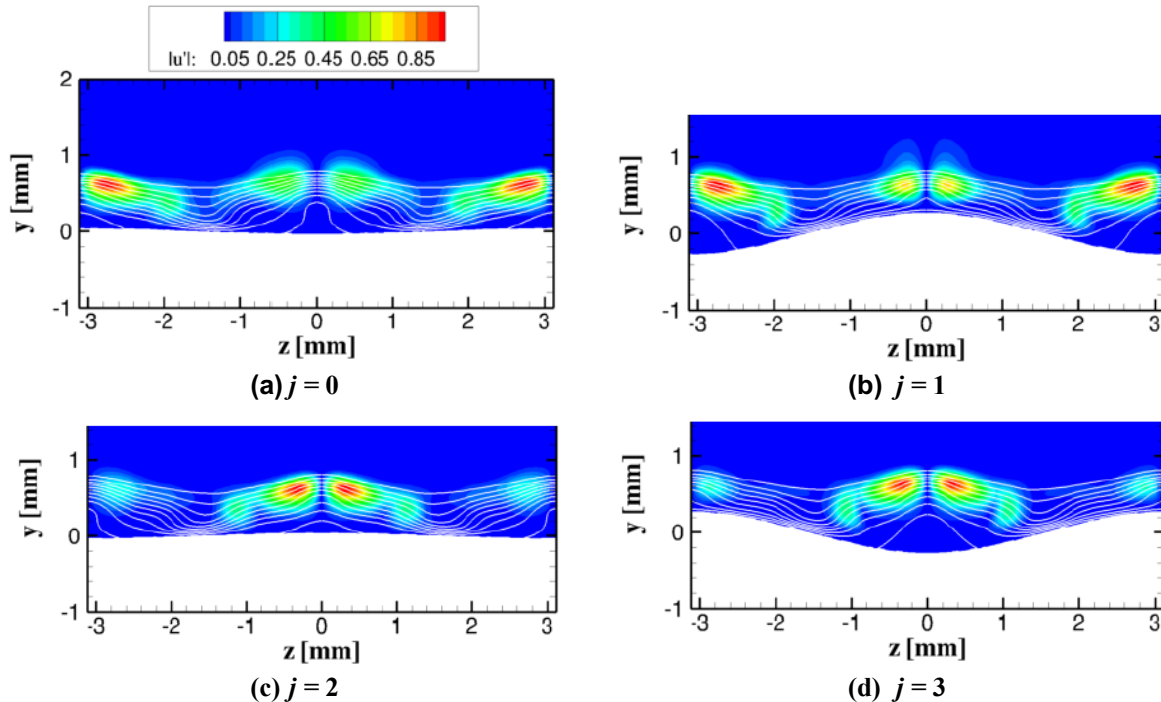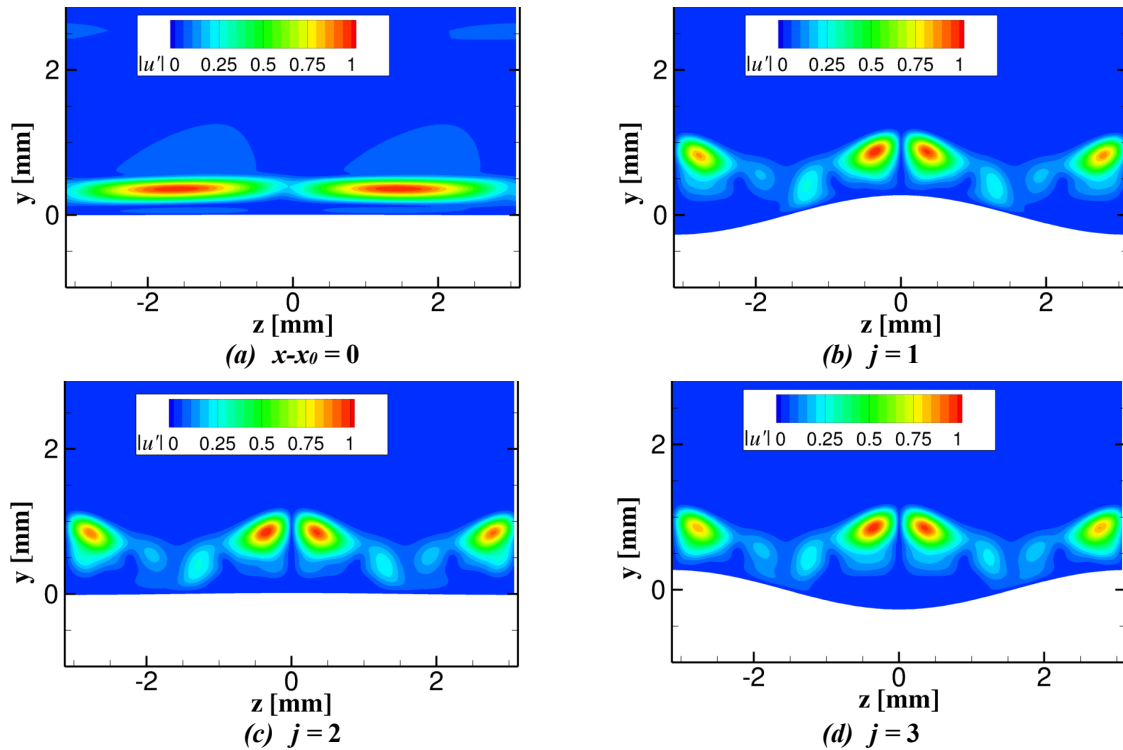

Figure 6. Mode shapes of $|u'|$ fluctuation associated with AA mode with $f = 50$ kHz. Line contours in white correspond to basic state u-velocity distribution across the wake.

B. DNS Results

The local instability analysis in the previous subsection provides useful insights into the nature of instabilities above the roughness patch. However, as discussed previously, that analysis does not account for the streamwise variations in the basic state, which occur on the shorter scale of λ_w, as opposed to the slower divergence of the unperturbed boundary layer flow on the scale of the distance from the plate leading edge. To overcome the limitation with respect to the stronger nonparallel effects within the length of the roughness patch, we next describe the preliminary findings from the DNS of disturbance evolution across the region of the wavy surface. The high-order DNS solver used here has previously been used to compute a similar evolution of high-frequency secondary instabilities of stationary crossflow modes in the boundary layer flow over a yawed cone.[25,26] A detailed description of the governing equations and their numerical discretization is given by Wu et al.[27] The inviscid fluxes from the

governing equations are computed by using a seventh-order weighted essentially nonoscillatory (WENO) finite-difference scheme introduced by Jiang and Shu;[28] but the solver also allows the use of limiters that have been optimized to reduce the numerical dissipation. Both an absolute limiter on the WENO smoothness measurement and a relative limiter on the total variation are employed simultaneously during the simulation. The viscous fluxes are discretized using a fourth-order central difference scheme and time integration is performed using a third-order low-storage Runge-Kutta scheme.[29]   In previous studies, this numerical code has also been applied to simulation of turbulence in hypersonic boundary layers[30] as well as laminar-turbulent transition due to crossflow instability in swept wing boundary layers.[31,32]   The lessons learned from these simulations were applied to develop the computational grid for the DNS computations described herein.

The computational domain for DNS has a spanwise extent of λ_z for simulations of the AA and SS modes and equal to $2\lambda_z$ for the SA and AS modes. The wall-normal extent of the computational domain extends well beyond the boundary-layer region, so as to allow an adequate decay of both stationary and nonstationary perturbations. A typical grid included 40 points within each streamwise wavelength of the roughness patch and 120 points across each spanwise wavelength. The wall-normal domain was resolved with 200 points with clustering within the boundary layer region. Additional simulations were performed in one case by halving the grid spacing in the wall normal direction and reducing the grid spacing in the other two directions by a factor of 1.5. Since the primary focus of the present work corresponds to the roughness patch region, the streamwise domain is truncated at $x \approx 0.11$ m, i.e., a small distance beyond the trailing edge of the roughness patch with $L_w/\lambda_w = 8.0$. The disturbances are introduced at the inflow boundary by using the mode shapes derived from oblique, first mode waves in the unperturbed boundary layer (Fig. 7(a)). The computed mode shape at the beginning of the roughness patch ($x-x_0 = 0$) in Fig. 7(a) closely resembles the antisymmetric disturbance corresponding to an oblique first mode wave with a spanwise wavelength equal to λ_z.

(a) $x-x_0 = 0$ *(b) $j = 1$*

(c) $j = 2$ *(d) $j = 3$*

Figure 7. Mode shapes of $|u'|$ fluctuation at the start of the roughness patch and within the last wavelength of the patch with $\lambda_w = 6.25$ mm, $k = 272$ μm, and $L_w/\lambda_w = 8.0$. Disturbance type corresponds to AA mode with $f = 50$ kHz. Streamwise stations in parts (b) through (d) correspond to $x = x_0 + L_w - \lambda_w (1 - j/4), j = 1$–3.

The computations of wake instability in Ref. [14] had shown that the most amplified disturbances in the wake region downstream of the roughness patch are of the AA mode type, and their frequencies are centered at approximately 50 kHz. Therefore, we first analyze the upstream evolution of an AA mode with $f = 50$ kHz across

American Institute of Aeronautics and Astronautics

the region of the roughness patch. Mode shapes of the computed $|u'|$ fluctuation at selected streamwise locations are shown in Fig. 7. The peak u' fluctuations at the beginning of the roughness patch ($x-x_0 = 0$) in Fig. 7(a) are found near $z/\lambda_z = \pm0.25$. However, as this disturbance propagates through the boundary layer flow above the roughness patch, the peak fluctuations migrate closer to the symmetry plane locations at $z/\lambda_z = 0$ and 0.5, respectively. The mode shapes toward the end of the roughness patch bear some similarities to the mode shapes predicted by the quasiparallel instability analysis (Fig. 6). However, one also observes certain noteworthy differences, particularly in regard to the relative importance of the peaks near $z/\lambda_z = 0$ and 0.5, respectively.

The amplification characteristics of the same AA mode above the roughness patch are shown in Fig. 8, wherein the N-factor is plotted as a function of normalized distance from the leading edge of the patch. Results are shown for two different lengths of the roughness patch, viz., $L_w/\lambda_w = 1.0$ and $L_w/\lambda_w = 8.0$, respectively. For convenience, the N-factors are computed with respect to the start of the roughness patch, i.e., $x-x_0 = 0$. Although not shown, results obtained from the fine grid simulation indicated almost no differences from the results shown here. The N-factor values for $L_w/\lambda_w = 8.0$ are generally larger than those in the $L_w/\lambda_w = 1.0$ case, indicating the strong destabilizing influence of the roughness patch on the first mode waves. Furthermore, the nonmonotonic variation in the slope of the N-factor curve for $L_w/\lambda_w = 8.0$ indicates the cyclic changes in the disturbance growth rate within the region of surface waviness. The DNS results confirm that the growth rate of the AA mode with $f = 50$ kHz remains positive throughout the length of the patch; however, the minimum growth rate within each wavelength of the roughness patch can be substantially smaller than the peak value of the growth rate. Such cyclic variation in the growth rate of a fixed frequency disturbance was also apparent in the quasiparallel predictions in Fig. 5.
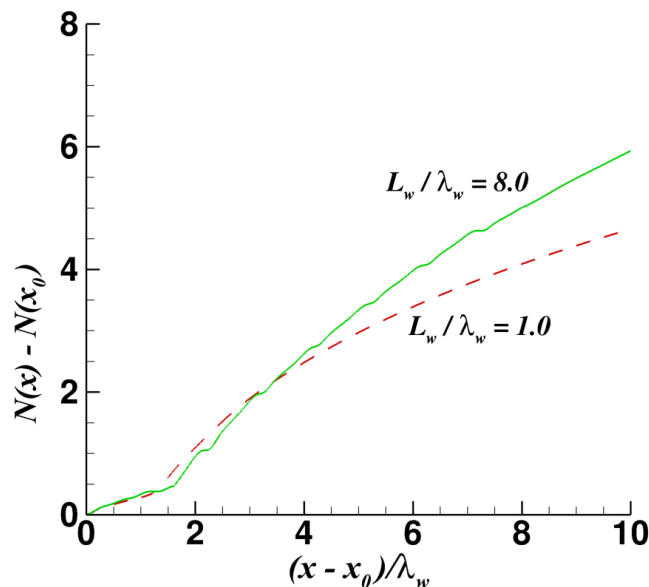
Fig. 8. N-factor evolution for AA mode with $f = 50$ kHz for two roughness patches of different lengths. The abscissa corresponds to normalized distance from the start of the roughness patch and the N-factor is normalized to be unity at $x - x_0 = 0$.

According to the results from Fig. 4, oblique first mode waves in the unperturbed boundary layer would amplify by a factor of approximately $exp(1.4)$ across the length of the roughness patch with $L_w/\lambda_w = 8.0$. In comparison, the DNS results with the roughness patch indicate that the AA mode at $f = 50$ kHz amplifies by a factor of nearly $exp(5.0)$ across the same distance, indicating an N-factor increment of 3.6 that represents the extra amplification above the wavy surface. Even though additional DNS computations are necessary to determine the maximum increment in N-factor across all possible disturbances, we can certainly conclude from Fig. 8 that the roughness patch region can contribute a significant extra disturbance growth ahead of the disturbance amplification process within the wake. Indeed, given the magnitude of the overall amplification of the AA mode until the end of the roughness patch with $L_w/\lambda_w = 8.0$, it is possible for the onset of transition to occur shortly downstream of the roughness patch, or perhaps, even within the length of the patch, if and when the incoming disturbance amplitudes

are relatively large such as those in a noisy wind tunnel environment. DNS computations to investigate this possibility are currently in progress.

Although not shown, additional DNS for AA modes had indicated comparable N-factors for disturbance frequencies of $f = 30$ kHz and $f = 75$ kHz, indicating a robust disturbance amplification across a relatively large band of frequencies. A significant growth above the roughness patch region was also noted for other disturbance types, such as the SS modes. However, given the large parameter space of the unstable modes, the results obtained until now are not comprehensive enough to judge which disturbances are likely to determine the N-factor envelope associated with the most amplified disturbances.

IV. Summary and Concluding Remarks

Numerical computations are performed to investigate the effects of extended surface waviness, or equivalently, a finite region of smooth-shaped, densely packed roughness elements in a Mach 3.5 flat plate boundary layer at the freestream conditions of a planned experiment in the Supersonic Low Disturbance Tunnel at the NASA Langley Research Center. Specifically, the present work extends the previously reported computations of instability development within the wake of the roughness patch by considering the disturbance growth characteristics over the roughness patch itself. Quasiparallel predictions for the evolution of instability modes within the roughness patch region were described in the preceding section. Preliminary findings based on the still ongoing computational study indicate that the flow above the roughness patch supports a group of low-frequency instability waves (peak amplification rates between 30 kHz and 100 kHz) that are analogous to the instability modes within the wake region, and another group of higher frequency modes (200 kHz to 300 kHz) that amplify within a narrow range of frequencies and spatial locations across a given streamwise wavelength of the roughness patch. The low-frequency modes overlap in frequency with the oblique, first mode instabilities of the unperturbed, flat plate boundary layer in the same range of streamwise locations. DNS results reveal that the roughness patch can lead to a significant increase in the amplification factor of the low-frequency modes, and that the increment in N-factor across the length of the roughness patch can be as large as $\Delta N \approx 3.6$ for selected modes above a roughness patch with $\lambda_w = \lambda_z = 6.25$ mm, $L_w/\lambda_w = 8.0$, and $k = 272$ μm. The relatively large N-factor increment indicates that transition onset predictions based on disturbance amplification within the wake region alone may result in a significant overestimation of the laminar flow length in such cases. Furthermore, differences in amplification factors over roughness patches of varying lengths and heights would lead to a variability in the N-factor correlation based on the wake instabilities alone. Finally, the DNS results also indicate a cyclic variation in the amplification characteristics above the wavy surface, which is indicative of the enhanced nonparallel effects within this region.

Since the preliminary DNS results presented in this paper are limited to a narrow range of disturbance parameters, the peak disturbance amplification above the roughness patch is likely to be even larger than the N-factor increment mentioned above. Additional DNS are necessary to ascertain the significance of the high-frequency modes ($f = 200$–300 kHz) indicated by the local stability analysis as well as to estimate the envelope of the most amplified disturbances in the presence of the roughness patch and to determine the characteristics of a potential laminar flow breakdown within the region of the surface waviness.

References

[1] Berry, S. A., Horvath, T. J., Greene, F. A., Kinder, G. R., and Wang, K. C., "Overview of Boundary Layer Transition Research in Support of Orbiter Return to Flight," AIAA Paper 2006-2918, June 2006.

[2] Van Driest, E. R. and McCauley, W. D., "The Effect of Controlled Three-Dimensional Roughness on Boundary-Layer Transition at Supersonic Speeds," *J. Aero. Sc.*, Vol. 27, No. 4, 1960, pp. 261–271.

[3] Casper, K., Wheaton, B., Johnson, H., and Schneider, S., "Effect of Freestream Noise on Roughness-Induced Transition at Mach 6," AIAA Paper 2008-4291, 2008.

[4] Schneider, S. P., "Effects of Roughness on Hypersonic Boundary Layer Transition," Journal of Spacecraft and Rockets, Vol. 45, No. 2, 2008, pp. 193–209.

[5]   Schneider, S. P., "Hypersonic Boundary-Layer Transition on Blunt Bodies with Roughness," AIAA Paper 2008-501, 2008.

[6]   Choudhari, M., Li, F., Paredes, P., and Chang, C.-L., "Boundary Layer Transition on Hypersonic Vehicles: Effects of Surface Roughness and Surface Blowing," Multiphysics Phenomena Analysis on Boundary Layer Stability in Hypersonic Regime - STO-AVT-289 Lecture Series, von Karman Institute for Fluid Dynamics, Sint-Genesius-Rode, Belgium, Sep. 18-20, 2017.

[7]   Choudhari, M., Li, F., Wu, M., Chang, C.-L., and Edwards, J. A., "Laminar Turbulent Transition behind Discrete Roughness Elements in a High-Speed Boundary-Layer," AIAA Paper 2010-1575, 2010.

[8]   Chou, A. and Kegerise, M., "Transition Induced by a Streamwise Array of Roughness Elements on a Supersonic Flat Plate," AIAA Paper 2017-4515, 2017.

[9]   Reda, D. C., "Correlation of Nosetip Boundary-Layer Transition Data Measured in Ballistics-Range Experiments," *AIAA Journal*, Vol. 19, No. 3, 1981, pp. 329–339.

[10] Reshotko, E. and Tumin, A., "Role of Transient Growth in Roughness-Induced Transition," *AIAA Journal*, Vol. 42, No. 4, 2004, pp. 766–770.

[11] Reda, D. C., Wilder, M. C., Bogdanoff, D. W., and Prabhu, D. K., "Transition Experiments on Blunt Bodies with Distributed Roughness in Hypersonic Free Flight," *Journal of Spacecraft and Rockets*, Vol. 45, No. 2, March-April 2008, pp. 210–215.

[12] Hollis, B., "Correlation of Recent and Historical Rough-Wall Transition Data on Hemispherical Nosetips," AIAA Paper 2017-3986, 2017.

[13] Muppidi, S. and Mahesh, K., "Direct Numerical Simulations of Roughness-Induced Transition in Supersonic Boundary Layers," *J. Fluid. Mech.*, Vol. 693, 2012, pp. 28–56.

[14] Choudhari, M., Li, F., and Paredes, P., "Effect of Distributed Patch of Smooth Roughness Elements on Transition in a High-Speed Boundary Layer," Presented at 48th AIAA Fluid Dynamics Conference, Atlanta, GA, June 25-29, 2018.

[15] Kimmel, R. L., Adamczak, D. A., Paull, A., Paull, R., Shannon, J., Pietsch, R., Frost, M., Alesi, H., "HIFiRE-1 Ascent-Phase Boundary-Layer Transition," *Journal of Spacecraft and Rockets*, Vol. 52, 2015, pp. 217-230.

[16] vulcan-cfd.larc.nasa.gov (last accessed April 17, 2018).

[17] van Albada, G. D., van Leer, B. and Roberts, W. W., "A Comparative Study of Computational Methods in Cosmic Gas Dynamics," *Astronomy and Astrophysics*, Vol. 108, 1982, pp. 76-84.

[18] Edwards, J. R., "A Low-Diffusion Flux-Splitting Scheme for Navier-Stokes Calculations," *Computer and Fluids*, Vol. 6, 1997, pp. 635-659.

[19] Litton, D., Edwards, J., and White, J., "Algorithmic Enhancements to the VULCAN Navier-Stokes Solver," AIAA Paper 2003-3979, 2003.

[20] Choudhari, M., Li, F., and Edwards, J. R., "Advanced Stability Analysis Pertaining to Roughness Effects on Laminar-Turbulent Transition in Hypersonic Boundary Layers," HYP/AAP Quarterly Bulletin, ed. S. Yoon, March 2008; also, AIAA Paper 2009-0170, Jan. 2009.

[21] Groskopf, G., Kloker, M. J., and Marxen, O., "Bi-global Secondary Stability Theory for High-Speed Boundary Layer Flows," In Proceedings of the Summer Program, Center for Turbulence Research, December 2008.

[22] De Tullio, N., Paredes, P., Sandham, N., and Theofilis, V., "Laminar-Turbulent Transition Induced by a Discret Roughness Element in a Supersonic Boundary Layer," *J. Fluid Mech.*, Vol. 735, 2013, pp. 613-646.

[23] Paredes, P., Choudhari, M., and Li, F., "Transition due to Streamwise Streaks in a Supersonic Flat Plate Boundary Layer," *Phys. Rev. Fluids*, Vol. 1, 2016, pp. 083601–1–23.

[24] Paredes, P., Choudhari, M., and Li, F., "Instability Wave-Streak Interactions in a Supersonic Boundary Layer," *J. Fluid Mech.*, Vol. 831, 2017, pp. 524–553.

[25] Choudhari, M., Li, F., Paredes, P., and Duan, L., "Nonlinear Evolution and Breakdown of Azimuthally Compact Crossflow Vortex Pattern over a Yawed Cone," AIAA Paper 2018-1823, 2018.

[26] Li, F., Choudhari, M., Paredes, P., and Duan, L., "High-Frequency Instabilities of Stationary Crossflow Vortices in a Hypersonic Boundary Layer," *Phys. Rev. Fluids*, Vol. 1, 2016, 053603.

[27] Wu, M. and Martin, M. P., "Direct Numerical Simulation of Supersonic Boundary Layer over a Compression Ramp," *AIAA Journal*, Vol. 45, No. 4, 2007, pp. 879–889.

[28] Jiang, G. S. and Shu, C. W., "Efficient Implementation of Weighted ENO Schemes," *J. Comp. Phys.*, Vol. 126, No. 1, 1996, pp. 202–228.

[29] Williamson, J., "Low-Storage Runge-Kutta Schemes," *J. Comp. Phys.*, Vol. 35, No. 1, 1980, pp. 48–56.

[30] Taylor, E. M., Wu, M., and Martin, M. P., "Optimization of Nonlinear Error Sources for Weighted Non-Oscillatory Methods in Direct Numerical Simulations of Compressible Turbulence," *J. Comp. Phys.*, Vol. 223, No. 1, 2006, pp. 384–397.

[31] Duan, L., Beekman, I., and Martin, M. P., "Direct Numerical Simulation of Hypersonic Turbulent Boundary Layers. Part 3: Effect of Mach Number," *J. Fluid. Mech.*, Vol. 672, 2011, pp. 245–267.

[32] Duan, L., Choudhari, M., and Li, F., "Direct Numerical Simulation of Crossflow-Induced Transition in a Swept Wing Boundary Layer," AIAA Paper 2013-2617, 2013.